



## Low-temperature CO oxidation at persistent low-valent Cu nanoparticles on TiO<sub>2</sub> aerogels



Paul A. DeSario<sup>a,\*</sup>, Catherine L. Pitman<sup>a,1</sup>, Daniel J. Delia<sup>a,2</sup>, Darren M. Driscoll<sup>b</sup>, Andrew J. Maynes<sup>b</sup>, John R. Morris<sup>b</sup>, Ashley M. Pennington<sup>a,1</sup>, Todd H. Brintlinger<sup>c</sup>, Debra R. Rolison<sup>a</sup>, Jeremy J. Pietron<sup>a</sup>

<sup>a</sup> Chemistry Division (Code 6100), U.S. Naval Research Laboratory, 4555 Overlook Avenue SW, Washington, D.C., 20375, USA

<sup>b</sup> Department of Chemistry, Virginia Tech, Blacksburg, VA, 24061, USA

<sup>c</sup> Materials Science and Technology Division (Code 6300), U.S. Naval Research Laboratory, 4555 Overlook Avenue SW, Washington, D.C., 20375, USA

### ARTICLE INFO

**Keywords:**  
CO oxidation  
Aerogels  
Copper nanoparticles  
Reducing oxide supports

### ABSTRACT

We exploit interfacial charge transfer from titania (TiO<sub>2</sub>) to copper (Cu) to design catalytic Cu/TiO<sub>2</sub> composite aerogels that shift the chemical state of Cu nanoparticles away from Cu<sup>2+</sup>, making them highly active for low-temperature CO oxidation. The high degree of interfacial contact between ~2–3 nm-diameter Cu particles and the networked ~10 nm-diameter TiO<sub>2</sub> particles in ultraporous aerogel stabilizes a high ratio of Cu<sup>0/1+</sup>:Cu<sup>2+</sup>. The reduced nature of Cu in Cu/TiO<sub>2</sub> aerogels is evidenced by a strong surface plasmon resonance in its diffuse reflectance UV-vis spectrum, by its X-ray photoelectron spectral features, and by infrared spectroscopic evidence of CO binding at the catalyst surface. In contrast, when larger diameter (~50–60 nm), non-networked TiO<sub>2</sub> particles are used to support Cu nanoparticles, the single planar nanoscale interface between Cu and the support particle stabilizes a much lower fraction of low-valent Cu. The Cu<sup>0/1+</sup> speciation stabilized within the aerogel catalyzes low-temperature CO oxidation (< 100 °C) at high conversion rates and does not necessitate high-temperature activation in a reducing gas stream—performance that the non-networked catalyst cannot meet. Our work demonstrates how nanoscale interfacial materials design can be exploited to create active Cu nanoparticle-based catalysts that are stable under practical conditions.

### 1. Introduction

Supported copper nanoparticles (Cu NPs) are active for low-temperature heterogeneous oxidation catalysis, including oxidation of carbon monoxide [1–8]. Carbon monoxide (CO) oxidation is an important reaction for energy conversion and storage, industrial applications, and treatment of exhaust streams. While the high activity of precious metal catalysts (e.g., Pd, Pt, Au) has made them the default choice in industrial CO oxidation, Cu, as a cheaper and more abundant alternative, would be attractive if catalytic Cu could demonstrate high activity and durability.

The oxidation state of supported Cu is critically important for low-temperature (< 100 °C) CO oxidation. Generally, conversion rates are higher and activation energy ( $E_a$ ) is lower for Cu<sup>1+</sup> and Cu<sup>0</sup> than for Cu<sup>2+</sup> [3–7]; low-valent Cu can exhibit conversion rates and  $E_a$  competitive with precious metals [3]. A primary CO oxidation pathway is

the Langmuir–Hinshelwood mechanism, involving adsorption and activation of CO at Cu<sup>0</sup> or Cu<sup>1+</sup> sites combined with activation of gas-phase O<sub>2</sub> at the oxide [3]. Alternate pathways include rate-determining steps such as reduction of inactive Cu<sup>2+</sup> to active Cu<sup>1+</sup> by excess gas-phase CO [3], and participation of lattice oxygen induced by gas-phase O<sub>2</sub> (demonstrated by <sup>18</sup>O isotope exchange) [8]. A mixture of Cu<sup>0/1+</sup> oxidation states may also be beneficial given that a two-Cu site mechanism has been spectroscopically indicated for low-temperature CO oxidation that requires neighboring Cu sites of two different oxidation states [7].

Cu is prone to oxidation, especially on the nanoscale [9], and the more catalytically active oxidation states are difficult to stabilize. Reduced Cu is commonly prepared by heat treating in an aggressively reducing atmosphere [8,10] or by keeping the catalyst under ultrahigh vacuum conditions [1–3]. While these approaches have enabled investigation of the catalytic activity of low-valent Cu, strategies must be

\* Corresponding author.

E-mail address: [paul.desario@nrl.navy.mil](mailto:paul.desario@nrl.navy.mil) (P.A. DeSario).

<sup>1</sup> NRC Postdoctoral Fellow at the U.S. Naval Research Laboratory.

<sup>2</sup> Pathways student at U.S. Naval Research Laboratory.

developed that stabilize the more active, reduced forms of Cu and do so on supports that are rugged under real-world conditions.

Metal-oxide supports play an important role in influencing the oxidation state of Cu. Some oxides such as  $\text{SiO}_2$  are passive supports and neither participate in adsorption/activation of reactants nor affect the chemical speciation of supported nanoparticles [5]. In contrast, reducing oxides such as titania ( $\text{TiO}_2$ ) can influence Cu speciation and chemistry. Electron donation from  $\text{TiO}_2$  to higher work function  $\text{CuO}$  is energetically favorable [4,10,11]. Defects such as oxygen vacancies create  $\text{Ti}^{3+}$  sites in  $\text{TiO}_2$  that donate electrons to supported Cu [5,12,13]. This charge transfer is highly localized near the oxide||metal interface [4,10], and as a result, fully or partially reduced Cu is typically localized near the interface. In addition to electron transfer, formation of a mixed  $\text{TiCuO}_x$  phase, which has been characterized at the interfacial region between  $\text{TiO}_2$  clusters deposited onto a  $\text{Cu}_2\text{O} < 111 >$  film, can thermally and chemically stabilize highly reactive  $\text{Cu}^{1+}$  sites and limit the oxidation of  $\text{Cu}_2\text{O}$  [14].

We further exploit the reducing nature of  $\text{TiO}_2$  supports by using a materials design that increases Cu|| $\text{TiO}_2$  interfacial contact, which in turn stabilizes a high fraction of the reduced Cu species favorable for CO oxidation. We recently demonstrated that the multiple points of contact that are created after photodepositing 2–3-nm Cu NPs at a  $\text{TiO}_2$  aerogel poises Cu NPs primarily in a mixed  $\text{Cu}^0/\text{Cu}^{1+}$  valence [15]. Unlike traditional particulate supports, aerogels comprise  $\sim 10$  nm covalently bonded particles co-continuous with mesoporous void [16]. The reduced nature of  $\text{TiO}_2$  aerogel-supported Cu NPs is made evident by the strong surface plasmon resonance (SPR), characteristic of a high content of metallic Cu, in the visible absorption spectrum of Cu/ $\text{TiO}_2$  aerogel. The Cu NPs remain reduced even after long-term exposure to ambient air, as demonstrated by the persistence of the SPR feature [15].

While we previously characterized photoelectrochemical reactivity at Cu/ $\text{TiO}_2$  aerogels, we have not yet established how the oxidation state of supported Cu particles—as influenced by its interfacial arrangement with  $\text{TiO}_2$ —impacts activity in thermal catalysis. Herein, we compare the CO oxidation activity of two Cu/ $\text{TiO}_2$  composites with divergent nanoscale Cu|| $\text{TiO}_2$  interfacial structures—aerogel vs. a traditional, non-networked catalyst support. We also investigate how the oxidation state of  $\text{TiO}_2$ -supported Cu nanoparticles is affected by photo-assisted reduction at different interfaces. Our results demonstrate how interfacial materials design creates Cu nanoparticle-based oxidation catalysts that are active at low temperatures and stable under practical conditions.

## 2. Experimental

### 2.1. $\text{TiO}_2$ aerogel synthesis

Titania aerogels were synthesized using a sol–gel method described by Dagan and Tomkiewicz [17]. A solution of 2.5 g of titanium isopropoxide (Alfa-Aesar) and 3.9 g of ethanol (the Warner-Graham company) was added to a mixture of 0.39 g of 18  $\text{M}\Omega$  cm  $\text{H}_2\text{O}$ , 4.0 g of ethanol and 0.08 g of nitric acid (Fisher). The solution was allowed to gel and cure overnight. The wet gel was then rinsed with acetone multiple times to exchange the pore-filling fluid before loading into a supercritical dryer. The acetone-infused gels were exchanged with  $\text{CO}_2$  at 10 °C multiple times before heating to 41 °C (above the critical temperature of  $\text{CO}_2$ ) and subsequently venting. The as-prepared aerogels are amorphous and were calcined at 425 °C in air (2 °C min<sup>−1</sup> ramp and cool, 4 h dwell) to crystallize the anatase phase.

### 2.2. Copper deposition onto $\text{TiO}_2$ supports

Copper was deposited onto  $\text{TiO}_2$  supports—aerogels and commercially available nanoparticulate anatase  $\text{TiO}_2$  (American Instrument Company, Inc.)—in a manner similar to that described by Wu et al [7]. Copper nanoparticles were deposited in slurries containing 150 mg of

$\text{TiO}_2$  dispersed in a 9:1 (vol: vol) water/ethanol solution containing 2 mM  $\text{Cu}(\text{NO}_3)_2$  (Sigma-Aldrich, 98%). The mass ratio of  $\text{Cu}^{2+}$  to  $\text{TiO}_2$  in the slurry is  $\sim 1:10$ . The solution pH was adjusted to 9.5  $\pm$  0.5 by adding drops of 1 M HCl or 1 M NaOH. The slurry was purged with Ar and continuously stirred. Deposition was initiated by impregnation in the dark for 1 h or by photodeposition under illumination for 24 h with a broad spectrum 450 W Xe arc lamp (Newport-Oriel). The slurries were then centrifuged and rinsed with water a total of 10 times before drying in air at 80 °C overnight.

### 2.3. Physical, structural, and chemical characterization

Brunauer–Emmet–Teller (BET) surface area and Barrett–Joyner–Halenda (BJH) pore size distributions were obtained from nitrogen ( $\text{N}_2$ ) physisorption isotherms (Micromeritics ASAP2020). Isotherm data were fitted with Micromeritics DFT software using a density functional theory model assuming cylindrical pore geometry. High-angle annular dark field (HAADF) images were obtained for Cu/ $\text{TiO}_2$  catalysts using an aberration-corrected scanning transmission microscope (ac-STEM, Nion UltraSTEM-200X) operating at 60 kV with  $\sim 100$  pA current and 120 pm nominal probe size. Samples were prepared for TEM analysis by sonicating and suspending in isopropyl alcohol, and drop-casting onto carbon-coated TEM grids.

The X-ray photoelectron spectroscopy (XPS, Thermo Scientific K-Alpha, Al-K $\alpha$  source) data were collected using a flood gun to minimize charging. Peak fitting and quantification were performed with the Avantage software. All binding energies were referenced to adventitious carbon at 284.8 eV. Smart background was subtracted from all spectra and peaks were fit with a 30% mixed Gaussian-Lorentzian function. The  $\text{Cu}2p_{3/2}$  envelope was fit with a  $\text{Cu}^{0/1+}$  component at 932.5  $\pm$  0.2 eV and a  $\text{Cu}^{2+}$  component with a binding energy separation of  $+1.8 \pm 0.2$  eV (934.3  $\pm$  0.2). The full width half maximum of the  $\text{Cu}^{0/1+}$  and  $\text{Cu}^{2+}$  components were constrained to  $< 2$  eV and  $< 2.5$  eV, respectively. Comparative Cu:Ti intensity ratios were determined by X-ray fluorescence (XRF) spectroscopy with a ThermoScientific Quant'X XRF in the Mid Zb range. Diffuse reflectance UV–vis absorption spectra were recorded using a Perkin Elmer 1050 spectrometer equipped with a 60 mm integrating sphere and converted to Kubelka–Munk units. The wavelength maxima of extinction features were determined from the first derivative of the diffuse-reflectance spectra. The X-ray diffraction (XRD) patterns were recorded with a Rigaku SmartLab (40 kV, 44 mA, 2°min<sup>−1</sup> scan speed) and average particle diameter was estimated by the Scherrer equation.

### 2.4. Infrared spectroscopy

Infrared spectroscopic studies of CO adsorption were performed in a stainless-steel high-vacuum reactor cell with a base pressure of  $1 \times 10^{-8}$  Torr. The Cu/ $\text{TiO}_2$  composite aerogels (Cu/Aero),  $\text{TiO}_2$  aerogel, and Cu/commercial anatase particle composites (Cu/CP) samples were all pressed into a tungsten mesh, which was then secured onto a precision manipulator. Manipulation of the sample holder allows for each sample to be exposed to the same gaseous and thermal environments for comparison between materials. For high-temperature thermal treatments, resistively heated copper rods were affixed to the sample mesh and attached to an external power supply. Each sample was thermally treated at 150 °C in vacuum to effectively remove weakly bound surface adsorbates. For low-temperature CO adsorption experiments, a liquid nitrogen cold trap was used to cool each sample to 180 K. A K-type thermocouple was attached directly to the tungsten mesh, within 3 mm of the samples, to monitor sample temperature. Details of the high-vacuum cell can be found in a previous study [18]. An FTIR spectrometer with an external MCT-A detector (Thermo, Nicolet Nexus 470 FTIR, resolution 2 cm<sup>−1</sup>) couples to the vacuum chamber to provide the in situ infrared spectroscopic measurements. Samples were exposed to 300 mTorr of CO (99.3% purity, Airgas

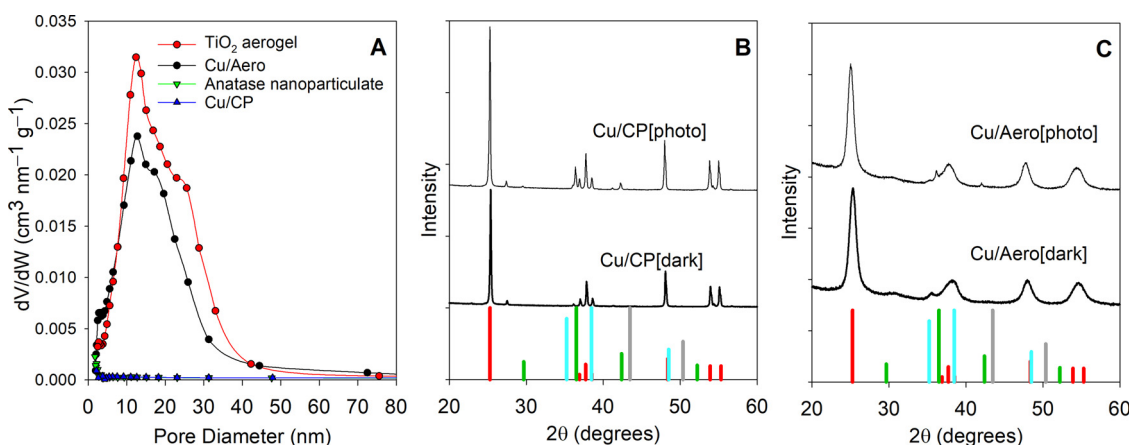


**Fig. 1.** A) Differential pore size distribution of anatase TiO<sub>2</sub> aerogels and commercial anatase nanoparticles before and after Cu deposition; X-ray diffraction patterns for B) Cu/CP and C) Cu/Aero composites. red: anatase TiO<sub>2</sub> (JCPDS# 01-075-2544); green: Cu<sub>2</sub>O (JCPDS# 01-073-6237); cyan: CuO (JCPDS# 00-044-0706); gray: Cu (JCPDS# 00-001-1241). (For interpretation of the references to colour in this figure legend, the reader is referred to the web version of this article).

CP300) at 180 K.

## 2.5. CO oxidation

Carbon monoxide (CO) oxidation was performed at 1 atm in a fixed-bed continuous flow reactor housed in a programmable ceramic tube oven. Reaction conditions, including catalyst weight loading, partial pressure of reactant gases, and total flow rate were established such that heat and mass transport effects could be ignored and CO conversions < 15% could be quantified in order to extract meaningful kinetics data [5,7,19,20]. The Cu/TiO<sub>2</sub> catalyst was diluted with TiO<sub>2</sub> aerogel (12.5 mg and 37.5 mg, respectively) to limit conversion. The 50 mg catalyst bed was packed in a glass tube (3/8" OD, 0.22" ID) in between a small amount of glass wool. A K-type thermocouple was affixed to the outside of the tube at the location of the packed catalyst bed and interfaced with a digital temperature controller (Barnant Company). A temperature differential between that measured by the thermocouple at the outer wall of the reactor and that inside the reactor is a possible source of error in our determination of activation energy ( $E_a$ ), however, the reactor wall is only 0.155" thick, so a significant temperature gradient should not arise. By our estimation,  $E_a$  is relatively insensitive to minor changes in temperature (only  $\sim 0.3 \text{ kJ mol}^{-1}$  per degree of temperature differential), and we factor in a 1°K uncertainty into the standard error of our  $E_a$  values (Table 2). The current through the heating element was measured with an Extech Instruments 381,275 Multiscope connected in series, where the current was recorded by computer and integrated over 5 min.

A gas feed comprising 1% CO (Airgas, 10,000 ppm) and 20% O<sub>2</sub> (Keen, 4.4. grade, 200,000 ppm) in He carrier (Praxair, UHP grade) was supplied at 50 mL min<sup>-1</sup>; all gases were controlled by digital mass flow controllers (Aalborg). The gas flow rate and concentration of CO were chosen such that the total CO conversion was always  $< 10^{-5} \text{ mol cm}^{-3} \text{ s}^{-1}$  in order to minimize mass- and heat-transport effects [20,21]. Gas head-space velocity (GHSV) at 50 mL min<sup>-1</sup> was approximately 20,000 h<sup>-1</sup> based on the volume of the 50 mg plug.

Catalyst beds were first activated in an anoxic gas stream of 1% CO in He while ramping to 150 °C at 10 °C min<sup>-1</sup> and then dwelling for 30 min. The O<sub>2</sub> flow was then initiated and temperature held at 150 °C for an additional 30 min. Temperature was then decreased stepwise while dwelling at each step for 20 min, until a temperature was reached where CO conversion was too low to quantify ( $\sim < 3\%$ ). The temperature was then increased stepwise to 150 °C. At each temperature step, 100-μL aliquots of the gas stream were sampled with a gas-tight syringe (Hamilton) from sample ports upstream and downstream of the catalyst plug and injected into a gas chromatograph (Shimadzu GC-

2010) equipped with a thermal conductivity detector and ShinCarbon column (Restek ST 100/120). The difference in peak area of multiple upstream and downstream injections at each temperature were averaged to quantify fractional conversion of CO. Duplicate (or more) packed catalyst beds were compared for each catalyst and plugs were temperature cycled twice in order to characterize catalyst aging.

## 3. Results and discussion

### 3.1. Influence of support architecture and illumination on Cu deposition at TiO<sub>2</sub>

We deposited Cu nanoparticles on two structurally divergent expressions of anatase TiO<sub>2</sub> to compare how interfacial arrangement impacts Cu oxidation state and subsequently dictates activity of thermal CO oxidation. We also include a dark, wet impregnation method to extend our synthetic approach beyond that used in our previous study in which we strictly used photoreductive deposition of Cu<sup>2+</sup> salts and applied different deposition times [15]. Contrasting activity between light and dark fabrication methods has yielded more detailed insight into the effects of TiO<sub>2</sub> mesoscale structure on Cu NP oxidation state. Aerogel supports—formed through sol-gel synthesis followed by supercritical drying and calcination at 425 °C—comprise a high surface area network ( $\sim 130\text{--}150 \text{ m}^2 \text{ g}^{-1}$ ) of covalently bonded  $\sim 10\text{-nm}$  diameter anatase nanocrystallites continuous with a network of meso and micropores (Fig. 1, Table 1, Fig. 2a). The large void volume of anatase TiO<sub>2</sub> aerogels ( $0.60 \text{ cm}^3 \text{ g}^{-1}$ ) is mainly distributed among 4–30 nm diameter pores (Fig. 1) [15]. For contrast, we also supported Cu NPs on a low surface area ( $< 10 \text{ m}^2 \text{ g}^{-1}$ ), small void volume ( $0.05 \text{ cm}^3 \text{ g}^{-1}$ ), non-networked commercial anatase powder with an average crystallite diameter of 50–60 nm (Fig. 1, Table 1, Fig. 2b).

The same Cu photodeposition procedure was followed for aerogel or commercially available particulate supports (designated Cu/Aero [photo] and Cu/CP[photo], respectively). After Cu deposition onto aerogels, the total void volume is reduced by  $\sim 8\%$  with a similar reduction in surface area (to  $\sim 120 \text{ m}^2 \text{ g}^{-1}$ ), while the pore size distribution remains essentially unaffected (Fig. 1a). In addition to the anatase reflections, the XRD pattern includes reflections assigned to Cu, Cu<sub>2</sub>O, and CuO (Fig. 1b, c). Imaging of Cu/Aero and Cu/CP via scanning transmission electron microscopy using a high-angle annular dark-field detector (STEM-HAADF) reveals well-dispersed,  $\sim 2\text{--}3 \text{ nm}$  diameter Cu particles on the surface of TiO<sub>2</sub> aerogels and commercial nanoparticles (Fig. 2c, d). Whereas an individual commercial anatase particle supports multiple Cu nanoparticles, smaller-diameter anatase particles host fewer Cu nanoparticles.

**Table 1**Summary of physical and chemical characterization of Cu/TiO<sub>2</sub> composites.

Sample	Surface Area (m <sup>2</sup> g <sup>-1</sup> )	Void Volume (cm <sup>3</sup> g <sup>-1</sup> )	Anatase dia. <sup>c</sup> (nm)	wt. % Cu <sup>d</sup>	Satellite/Cu 2p <sup>e</sup>	Cu(0/I):Cu(II)	Cu:Ti (XRF)
Cu/Aero[photo] <sup>a</sup>	117–125	0.53–0.55	9–12	8.2–12.4	11–20%	1.4–2.2:1	0.61–0.62
Cu/Aero[dark]	134	0.53	9–12	12.4	19%	1.4:1	0.57
Cu/CP[photo] <sup>b</sup>	6.5–8.5	0.05–0.06	50–60	20–22	18–28%	0.7–0.9:1	0.56–0.60
Cu/CP[dark]	7.9	0.05	50–60	13	22%	0.9:1	0.11

<sup>a</sup> values are ranges for six replicate batches.<sup>b</sup> values are ranges for five replicate batches and exclude an outlier.<sup>c</sup> estimated using the FWHM of the Anatase (101) reflection and the Scherrer equation.<sup>d</sup> determined via XPS of intensity ratio of Cu 2p<sub>3/2</sub> to Ti 2p.<sup>e</sup> determined via XPS of intensity ratio of Cu(II) satellite to Cu 2p envelope. Satellite intensity is 30% of Cu 2p signal for commercial Cu(II) oxide standard.

The Cu/TiO<sub>2</sub> materials previously prepared by this photodeposition route yielded 10 wt% Cu, the expected loading from incorporating all of the Cu<sup>2+</sup> in the solution [15]. The constant Cu:Ti intensity ratio determined by XRF verifies that weight loading is stable across all batches of photodeposited Cu/TiO<sub>2</sub> regardless of the type of support (Table 1). The copper weight loading determined by XPS, however, suggests a ~20 wt% Cu loading for all Cu/CP[photo] samples, which is higher than the Cu:TiO<sub>2</sub> mass ratio in the reaction slurry. The lower surface area of the particulate supports inflates the amount of Cu present in surface-sensitive XPS analysis while XRF reveals a bulk loading that is comparable for both supports. Since aerogels have a much smaller particle size and a higher surface area to volume ratio, the weight loading measured by XPS analysis (8.0–12.4%) is in closer agreement with bulk techniques (Table 1).

Copper was also deposited on aerogel and commercial nanoparticle supports in the dark using a wet impregnation method (designated Cu/Aero[dark] and Cu/CP[dark], respectively) to assess the ability of each support to reduce nanoscale Cu in the absence of photogenerated electrons. This synthesis follows the photodeposition procedure except the slurry is stirred for 1 h while shielded from light rather than undergo irradiation for 24 h. The Cu/Aero[dark] samples show similar Cu loading by XPS and XRF to Cu/Aero[photo] (Table 1). While illumination was not needed to fully deposit ~10 wt% Cu on the high surface-area aerogel supports, Cu/CP[dark] had a significantly lower weight loading by XPS than Cu/CP[photo] (~12% vs. ~20%) and an XRF Cu:Ti intensity ratio 2.2 standard deviations below the mean (Table 1).

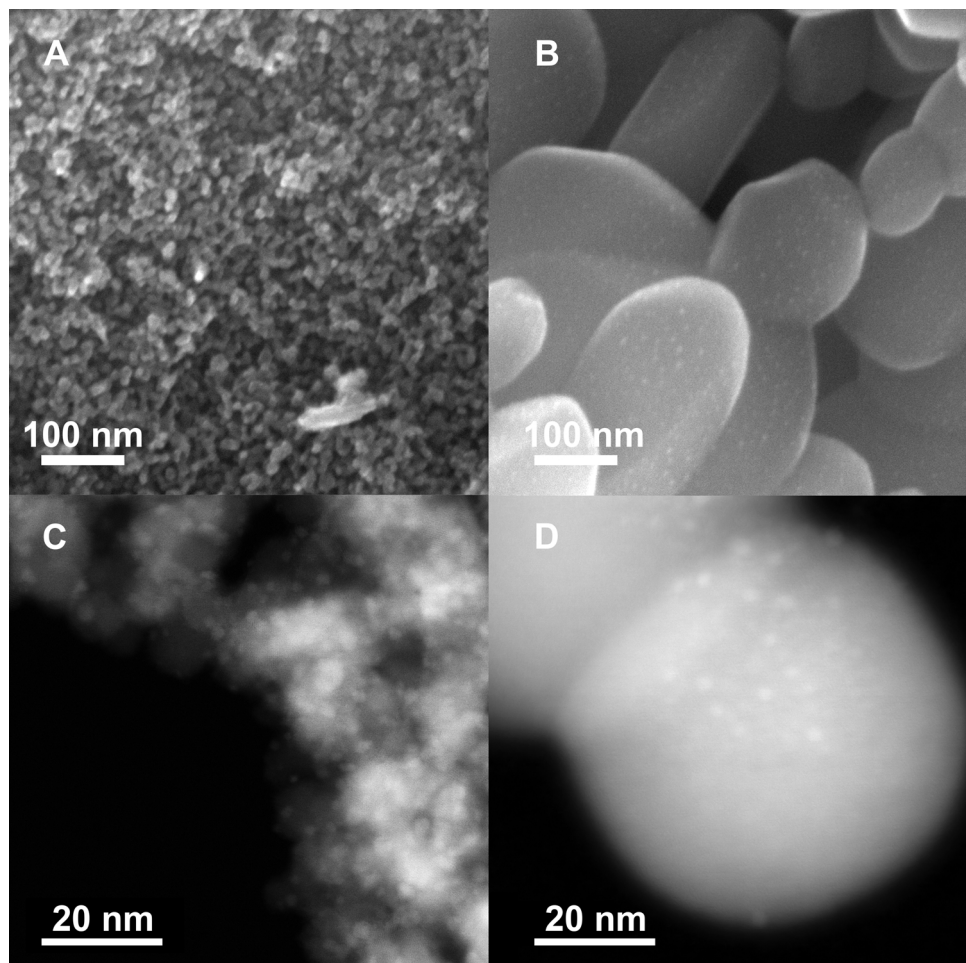


**Fig. 2.** Scanning electron micrographs of a) TiO<sub>2</sub> aerogel and b) commercial anatase nanoparticles and transmission electron microscopy high-angle annular dark field (STEM-HAADF) imaging of c) Cu/Aero and d) Cu/CP catalysts.

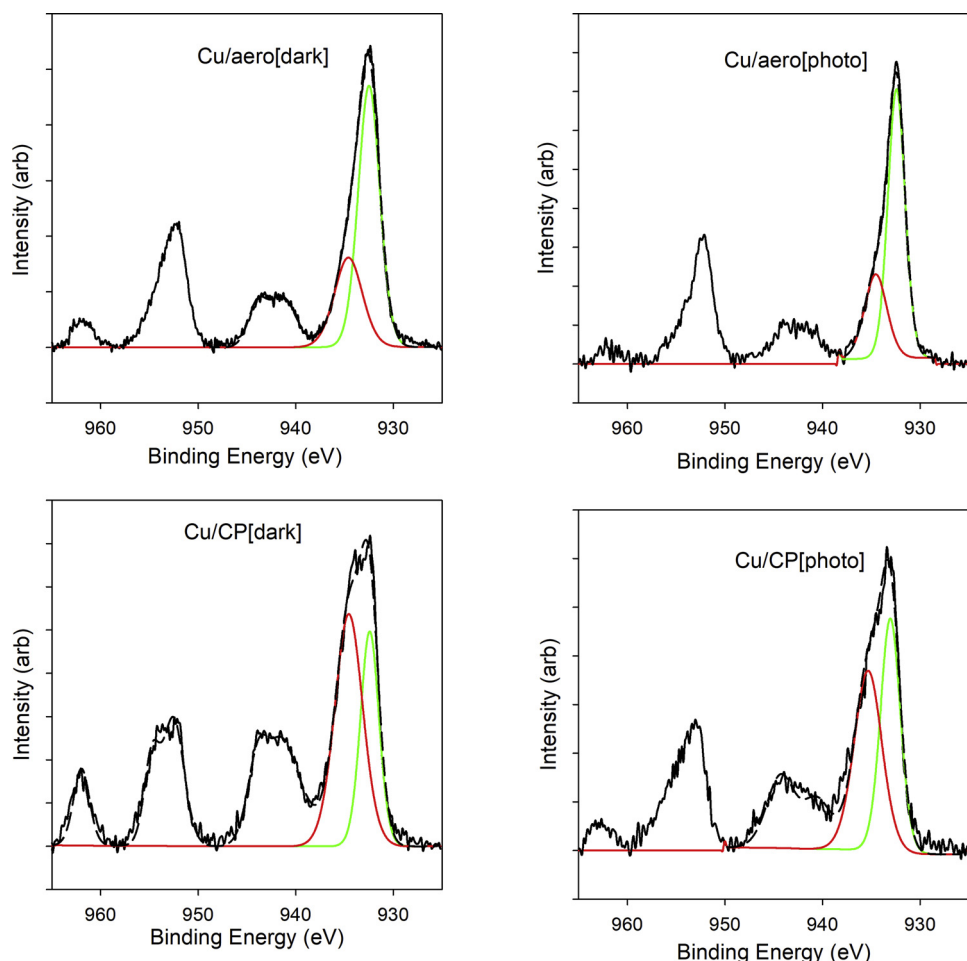


**Fig. 3.** The X-ray photoelectron spectra of the Cu 2p region for Cu/Aero and Cu/CP samples with the Cu 2p<sub>3/2</sub> envelope fitted to a Cu(I/0) peak at ~932.5 eV (green) and a Cu(II) peak at 934.5 eV (red) with the Cu(II) satellite centered between 940–945 eV. (For interpretation of the references to colour in this figure legend, the reader is referred to the web version of this article).

### 3.2. Influence of support and deposition procedure on surface and bulk Cu speciation

Both support type and deposition method influence the oxidation state of TiO<sub>2</sub>-supported Cu. The XPS analysis reveals that Cu is present in a mixed oxidation state on all Cu/TiO<sub>2</sub> composites. All samples display a Cu 2p<sub>3/2</sub> envelope with contributions from Cu<sup>0/1+</sup> at ~932.5 eV and Cu<sup>2+</sup> at ~934.5 eV (Fig. 3) [5,15,22]. In addition, a Cu<sup>2+</sup> shakeup satellite feature is present between 940 and 945 eV. While XPS can distinguish Cu<sup>2+</sup> from Cu<sup>1+</sup> or Cu<sup>0</sup> in the Cu 2p region, the lower valent states are indistinguishable. Differentiating Cu<sup>0</sup> from Cu<sup>1+</sup> is best done with the Cu LMM Auger peak, however, the overlap of this spectral region with the Ti 2s binding energy (BE), compounded by the higher relative intensity of Ti compared to Cu, precludes any relevant analysis in this region.

Instead we assess the weighted contribution of Cu<sup>0/1+</sup> to the Cu 2p<sub>3/2</sub> envelope to determine the relative proportions of Cu<sup>2+</sup> to low-valent Cu. We also compare the relative integrated intensity of the Cu<sup>2+</sup> satellite feature as a percentage of the total Cu 2p<sub>3/2</sub> integrated intensity. Six batches each of Cu/Aero[photo] and Cu/CP[photo] were synthesized: all Cu/Aero[photo] samples have a ratio of Cu<sup>0/1+</sup> to Cu<sup>2+</sup> > 1 (typically 1.4 to 2.7; Table 1 and Table S1), while most Cu/CP[photo] samples have a Cu<sup>0/1+</sup>:Cu<sup>2+</sup> ratio < 1 (ranging from 0.7 to 0.9; Table 1 and Table S2) with the exception of one outlier, discussed in more detail below. The relative intensity of the Cu<sup>2+</sup> satellite feature is higher for Cu/CP (18–28%) than Cu/Aero (11–20%) and approaches the 30% relative intensity assessed for a Cu(II) oxide standard,

indicating that a much higher proportion of Cu is oxidized when supported on Cu/CP than Cu/Aero. The Cu speciation is also significantly influenced by illuminating the Cu<sup>2+</sup>(aq) + TiO<sub>2</sub> slurry during deposition. On both supports, depositing Cu under illumination leads to a higher ratio of Cu<sup>0/1+</sup>:Cu<sup>2+</sup> as evidenced by a weaker Cu<sup>2+</sup> satellite feature and a greater contribution of Cu<sup>0/1+</sup> to the Cu 2p<sub>3/2</sub> envelope (Table 1, Fig. 3).

Differences in the Cu speciation between Cu/Aero and Cu/CP composites produce even starker contrasts in their diffuse reflectance UV-vis spectra (Fig. 4, Figure S1). The balance between Cu<sup>0</sup> and Cu<sup>1+</sup>, indistinguishable by XPS in the Cu 2p<sub>3/2</sub> region, is adjudicated by the presence or absence of an SPR. The spectra for Cu/Aero composites exhibit a broad feature centered near 760 nm, consistent with nanosized Cu structures whose dielectric environment has contributions from high refractive index media (such as Cu<sub>2</sub>O, CuO, and TiO<sub>2</sub>) [15,23–35]. The broadness of the SPR feature is attributed to polydispersity in Cu diameter, aspect ratio, and/or average dielectric environment surrounding each nanoparticle. The Cu SPR feature is not observed for any Cu/CP composites (Fig. 4, Figure S1), indicating that the Cu<sup>0/1+</sup> XPS assignment arises primarily from Cu<sup>1+</sup>. The presence of plasmonic Cu NPs in Cu/Aero indicates that the Cu<sup>0/1+</sup> XPS assignment has a contribution from Cu<sup>0</sup>.

Surface speciation of Cu nanoparticles in Cu/Aero and Cu/CP were characterized by IR spectroscopy using CO as a probe molecule (Fig. 5). The IR spectra were measured for Cu/Aero and Cu/CP at 180 K after a pretreatment at 150 °C in an anaerobic atmosphere (conditions similar to those used prior to CO oxidation reaction). The predominant

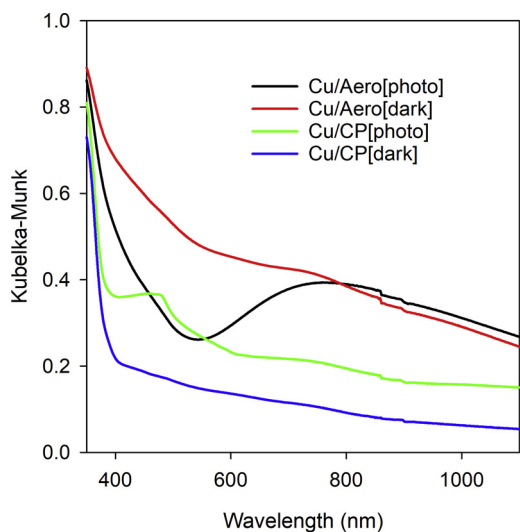


Fig. 4. Diffuse reflectance UV-vis spectroscopy for Cu/Aero and Cu/CP samples with spectral intensity converted to Kubelka–Munk units.

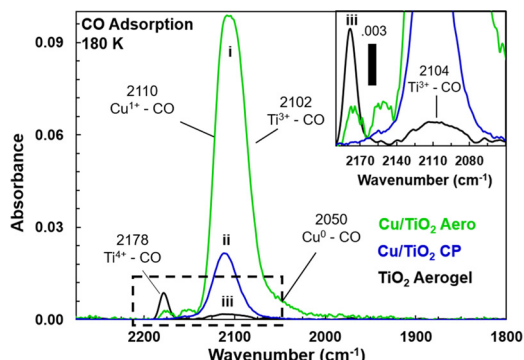


Fig. 5. Infrared spectroscopy of CO adsorption at 180 K at Cu/Aero (spectrum i, green trace), Cu/CP (spectrum ii, blue trace), and TiO<sub>2</sub> aerogel (spectrum iii, black trace) with inset displaying wavenumber region shown in black box. Samples were pretreated at 150 °C in reducing atmosphere prior to CO adsorption using the same protocol as performed prior to CO oxidation experiments. (For interpretation of the references to colour in this figure legend, the reader is referred to the web version of this article).

vibrational feature for Cu/Aero at 2108 cm<sup>-1</sup> is a confluence of both CO–Cu<sup>1+</sup> and CO–Ti<sup>3+</sup> adsorption sites, with the main component centered at 2110 cm<sup>-1</sup> attributed to CO–Cu<sup>1+</sup>. The small shoulder at 2050 cm<sup>-1</sup> is attributed to CO adsorption to metallic regions of the Cu nanoparticles (Cu<sup>0</sup>–CO), which are likely found at interfacial regions

surrounding the particles [7,15]. The feature associated with Cu<sup>0</sup> appears red shifted relative to the CO–Cu<sup>1+</sup> feature because the metallic Cu particles induce a greater back donation of electrons into the 2π\* antibonding orbitals of adsorbed CO molecules [36,37]. A Cu<sup>2+</sup>–CO binding mode (2195 cm<sup>-1</sup>) is only observed if the Cu/Aero catalyst is aggressively oxidized at 400 °C in an oxygen-rich atmosphere (Figure S2), otherwise, only reduced Cu species are present. The relative intensity of the Cu<sup>1+</sup>–CO and Cu<sup>0</sup>–CO modes reveals that the surface of the Cu nanoparticles in Cu/Aero is predominantly Cu<sup>1+</sup> while the majority of Cu<sup>0</sup> content resides in the core, giving rise to the SPR.

The weak SPR is observed for Cu/Aero[dark] that is significantly less prominent than the SPR observed for Cu/Aero[photo], but its existence is validated by a zero value in the first derivative of its diffuse-reflectance spectrum (Figure S3). The Cu/Aero[dark] sample also has a higher extinction than Cu/Aero[photo] extending from the anatase bandgap at ca. 400 nm to 550 nm, attributed to absorption from Cu<sub>2</sub>O (copper oxide diffuse-reflectance spectra are provided for reference in Figure S4). The qualitative strength of the Cu SPR and the relative prominence of Cu(I) oxide extinction from 400 to 550 nm for Cu/Aero[photo] and Cu/Aero[dark] are in good agreement with the respective quantitative assessment of Cu<sup>0/1+</sup>:Cu<sup>2+</sup> by XPS.

The diffuse-reflectance spectra of Cu/CP[photo] display features corresponding to the bandgap absorption of CuO (~850 nm, 1.45 eV) and Cu<sub>2</sub>O (~550 nm, 2.25 eV). In contrast, the spectrum of Cu/CP[dark] did not have a strong Cu<sub>2</sub>O absorption and had a lower extinction overall. The lower extinction and lack of a clear Cu<sub>2</sub>O feature are attributed to the lower weight loading of Cu and the fact that XPS reveals that this sample is predominantly Cu<sup>2+</sup>. The Cu<sub>2</sub>O reflection is more pronounced for Cu/CP[photo] than Cu/CP[dark] in their respective XRD patterns (Fig. 1), in agreement with the relative amounts of Cu<sup>0/1+</sup>:Cu<sup>2+</sup> assessed by XPS and diffuse-reflectance.

The dark, wet-impregnation synthesis yields further insight into the importance of the expression of the TiO<sub>2</sub> support: first, the high surface area of the aerogel results in high capacity for adsorption of Cu<sup>2+</sup> ions. During photodeposition, excitation of the TiO<sub>2</sub> bandgap ( $E_g = 3.2$  eV) leads to free electrons in the conduction band ( $E = -0.46$  eV vs. SHE) [38,39]; photogenerated holes in the TiO<sub>2</sub> valence band are scavenged by ethanol. Photogenerated electrons reduce adsorbed Cu<sup>2+</sup> to the observed Cu<sup>1+</sup> and Cu<sup>0</sup> oxidation states ( $E^\circ_{\text{Cu(II)/Cu(0)}} = +0.34$  V,  $E^\circ_{\text{Cu(II)/Cu(I)}} = +0.16$  V,  $E^\circ_{\text{Cu(I)/Cu(0)}} = +0.52$  V), thereby generating a higher fraction of reduced Cu than dark, wet impregnation. The Cu/CP[dark] composite expectedly yields predominately Cu<sup>2+</sup>—the only oxidation state possible if adsorption is the only process involved. The Cu/Aero[dark] catalyst, however, yields a sizable population of low-valent Cu, but does so without light as a driving force.

The defective nature of titania in aerogel form likely accounts for the electrons that lead to dark reduction of aerogel-adsorbed Cu<sup>2+</sup>. The interparticle junctions of networked TiO<sub>2</sub> are rich in Ti<sup>3+</sup> defect sites

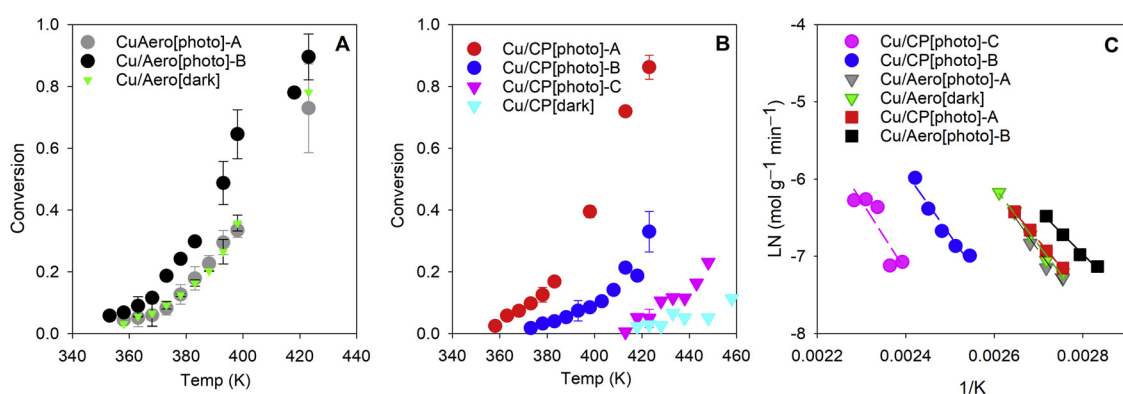


Fig. 6. Conversion vs. temperature for oxidation of carbon monoxide measured in a continuous flow reactor for 12.5 mg of A) Cu/Aero and B) Cu/CP mixed with 37.5 mg of TiO<sub>2</sub> aerogel in packed catalyst plugs; and C) Arrhenius plots made using data at 3–15% conversion of CO to CO<sub>2</sub>.

**Table 2**

Summary of physical and chemical characterization for Cu/Aero and Cu/CP catalysts prepared by wet impregnation or photodeposition.

Sample	Surface Area (m <sup>2</sup> g <sup>-1</sup> )	Void Volume (cm <sup>3</sup> g <sup>-1</sup> )	Satellite/Cu 2p <sub>3/2</sub> <sup>a</sup>	Cu <sup>0/1+</sup> :Cu <sup>2+</sup>	XRF Cu:Ti	E <sub>a</sub> (kJ mol <sup>-1</sup> )
Cu/Aero[photo]-A	125.3	0.54	15.8%	1.7:1	0.62	63.7 ± 3.2
Cu/Aero[photo]-B	117.3	0.55	20.2%	1.4:1	0.61	61.2 ± 3.6
Cu/Aero[dark]	133.8	0.53	18.8%	1.1:1	0.56	63.9 ± 3.5
Cu/CP[photo]-A	6.4	0.06	10%	2.6:1	0.59	62.4 ± 1.2
Cu/CP[photo]-B	7.9	0.06	18%	0.9:1	0.59	69.0 ± 4.3
Cu/CP[photo]-C	8.5	0.05	28.9%	0.6:1	0.57	75.8 ± 8.0
Cu/CP[dark]	7.9	0.05	22%	0.9:1	0.11	ND

<sup>a</sup> Satellite intensity is 30% of Cu 2p<sub>3/2</sub> intensity for Cu(II) oxide standard.

deriving from oxygen vacancies [40] and TiO<sub>2</sub> aerogel has a plethora of junctions inherent to the aerogel framework of covalently bound 10-nm TiO<sub>2</sub> nanoparticles. Electron-rich Ti<sup>3+</sup> centers are thermodynamically sufficient to directly reduce Cu<sup>2+</sup> ( $E^{\circ}_{\text{Ti(IV)/Ti(III)}} = 0.0 \text{ eV}$ ) [5] without photochemical assistance. Both Ti<sup>4+</sup> and Ti<sup>3+</sup> surface species in TiO<sub>2</sub> aerogels are evident by CO binding modes at 2177 cm<sup>-1</sup> for Ti<sup>4+</sup>–CO [7,15,41] and 2104 cm<sup>-1</sup> for Ti<sup>3+</sup>–CO. The Ti<sup>3+</sup> content is also confirmed in Cu/Aero by the asymmetric nature of the broad CO adsorption feature at 2125–2109 cm<sup>-1</sup> which has contributions from both Ti<sup>3+</sup>–CO and Cu<sup>1+</sup>–CO [42–44]. We expect the charge transfer between the TiO<sub>2</sub> aerogel and the Cu nanoparticle to promote the generation of oxygen vacancies at surrounding TiO<sub>2</sub> surface sites and thereby produce Ti<sup>3+</sup>. To confirm the presence of the Ti<sup>3+</sup> within the Cu/Aero, high-temperature (673 K) reducing and oxidizing treatments were applied and followed by subsequent low-temperature CO exposure. After high-temperature oxidation, the asymmetric CO adsorption feature observed for Cu/Aero transitions to a more symmetric vibrational feature centered at 2117 cm<sup>-1</sup> as Ti<sup>3+</sup> sites are blocked with reactive oxygen species and CO–Ti<sup>3+</sup> absorbance is quenched (Figure S2). Concurrently, some Cu<sup>1+</sup> is partially oxidized into a Cu<sup>2+</sup> while a slight increase in Ti<sup>4+</sup> concentration is also observed—further evidence of the loss of Ti<sup>3+</sup>. A similar, symmetric mode at 2117 cm<sup>-1</sup> is present for Cu/CP, which does not have measurable contributions from CO–Ti<sup>3+</sup>.

At a Cu diameter of 2–3 nm and TiO<sub>2</sub> diameter of 8–10 nm, each TiO<sub>2</sub> particle in the 10 wt.% Cu composites supports on average ~0.2 to 1.8 Cu particles (Fig. 2c). This average, approximate particle loading is easily accounted for by the number of TiO<sub>2</sub> particle–particle junctions in the aerogels and the expected surface defect density. The nanoparticulate anatase support, made up of 50–100-nm TiO<sub>2</sub> particles, has a much lower density of Ti<sup>3+</sup> defects (Fig. 5) and simultaneously each TiO<sub>2</sub> supports an average of ~48–380 Cu nanoparticles (Fig. 2d), thus the defect density in larger particles could be insufficient to accommodate 10 wt.% Cu loading. Evidence of Cu<sup>0</sup> is only found on the aerogel; even in Cu/CP samples with Cu<sup>0/1+</sup>:Cu<sup>2+</sup> ratios comparable to those of Cu/Aero, the Cu/CP shows no SPR evidence of persistent Cu<sup>0</sup>. As a support, the defect-rich interparticle junctions characteristic of the networked aerogel provide a persistent reducing environment to support metallic Cu.

### 3.3. CO oxidation: effect of TiO<sub>2</sub> support architecture and Cu oxidation state

We assessed how Cu speciation—as dictated by the expression of the TiO<sub>2</sub> support and the deposition conditions— influences catalytic activity. While changing the support and deposition route yields drastic differences in Cu speciation, we also compare the activity of replicate batches of Cu/Aero[photo] and Cu/CP[photo] samples (designated –A, –B, ... etc.) that express minor variations in Cu speciation.

Packed catalyst beds were activated at 150 °C in an anoxic gas mixture of CO and He. While Cu/TiO<sub>2</sub> catalysts are typically activated at higher temperature [4,5,7,8,10], we chose a more modest temperature in order to avoid Cu particle ripening which may occur at > 150 °C

(Figure S5). After activation, TiO<sub>2</sub> aerogel-only catalyst beds show no CO conversion, even up to 250 °C. Conversion of CO is only observed when Cu/Aero or Cu/CP is added to the catalyst bed. For all catalysts, a stoichiometric amount of O<sub>2</sub> is consumed along with CO (verified by gas chromatography) according to Eq. 1.



Conversion vs. temperature trends are nearly identical for increasing and decreasing temperature excursions (Figure S6). The absence of a hysteresis loop in a 0.5% CO reaction stream indicates localized self-heating is minimal under our reaction conditions and that the catalyst is likely not undergoing significant changes in oxidation state over the course of the experiment [45–48]. The importance of self-heating is assessed by monitoring current output from the heating element at different partial pressures of CO. With an 8% CO feedstream, the catalyst bed does not cool below 80 °C and conversion of CO to CO<sub>2</sub> remains > 95%. At high CO partial pressure, current output is minimal at temperatures < 100 °C indicating self-heating is responsible for the observed temperatures. When the partial pressure of CO is decreased, self-heating is insignificant and reaction temperature is then controlled by the heating element (Figure S7).

Duplicate packed catalyst beds prepared from the same catalyst sample show nearly identical reactivity, indicating that packing variability in preparing the catalyst bed has minimal impact on our results. Conversion of CO remained constant after ~8 h of dwell at a single temperature, and catalyst beds that were re-evaluated after initial usage exhibit near identical reactivity on repeated uses (Figure S6). Whereas rapid declines in activity can signify that Cu is oxidizing under the reaction conditions [14], the relative stability of our Cu/TiO<sub>2</sub> catalysts indicates that our catalysts resist oxidation. The oxidation state of Cu/Aero and Cu/CP catalyst is assessed by XPS after CO oxidation reaction (Figure S8) and the Cu<sup>0/1+</sup>:Cu<sup>2+</sup> ratio for Cu/Aero catalyst is constant before and after CO oxidation while the Cu/CP catalyst becomes slightly more reduced. The stability of the catalyst under reaction conditions is also verified by the fact that low-valent Cu<sup>1+</sup> and Ti<sup>3+</sup> remain at the surface of Cu/Aero after thermal treatment at 150 °C in oxygen-rich atmosphere, and it is only after a much more aggressive thermal oxidation at 400 °C that a small portion of Cu<sup>1+</sup> was converted to Cu<sup>2+</sup> while the CO–Ti<sup>3+</sup> mode is diminished (Figure S2).

The Cu/CP catalysts generally need higher temperatures to achieve the same CO conversion as Cu/Aero (Fig. 6). To obtain CO conversion above our limit of detection (~3%), Cu/Aero requires temperatures > 70–80 °C while Cu/CP requires even higher temperature (80–150 °C). The least active expression of Cu/TiO<sub>2</sub> is Cu/CP[dark] for which detectable CO conversion necessitates temperatures > 150 °C.

Activation energy (E<sub>a</sub>) is determined from Arrhenius plots using data between 3 and 15% conversion (Fig. 6c, Table 2). The highest E<sub>a</sub> (~76 kJ mol<sup>-1</sup>) was observed for Cu/CP[photo]-C, which has the highest Cu<sup>2+</sup> content of all catalysts tested: its XPS Cu<sup>2+</sup> satellite intensity is 29% of the Cu 2p<sub>3/2</sub> envelope intensity, almost identical to that measured for fully oxidized CuO (30%, Table 2), and it has the most obvious evidence of CuO content in its diffuse-reflectance spectrum (Figure S1). The E<sub>a</sub> measured for Cu/CP[photo]-C is consistent

with the value of  $16.7 \pm 0.5$  kcal mol<sup>-1</sup> (68–72 kJ mol<sup>-1</sup>) reported for CO oxidation at CuO [3].

Both Cu/CP[photo]-A and -B have a lower  $E_a$  than Cu/CP[photo]-C indicating a mechanistic shift for oxidation with increased low-valent Cu content (Fig. 6, Table 2). The  $E_a$  for Cu/CP[photo]-A and Cu/CP[photo]-B are consistent with the value of  $13.9 \pm 0.5$  kcal mol<sup>-1</sup> (56–60.3 kJ mol<sup>-1</sup>) reported for CO oxidation at Cu<sub>2</sub>O [3]. The trends in oxidation activity as Cu<sup>2+</sup> content decreases is consistent with multiple reports indicating that fully oxidized Cu<sup>2+</sup> is the least active form of Cu for CO oxidation [3–5,7].

While CO oxidation activity for Cu/CP was greatly enhanced by photodeposition and the resulting increase in Cu<sup>0/1+</sup>:Cu<sup>2+</sup>, the Cu/Aero catalysts do not show a strong correlation between Cu<sup>0/1+</sup>:Cu<sup>2+</sup> and CO oxidation behavior. The increased Cu<sup>0/1+</sup>:Cu<sup>2+</sup> in Cu/Aero[photo] vs. Cu/Aero[dark], which arises with increased Cu<sup>0</sup> content evidenced by the enhanced SPR feature, does not change the  $E_a$  or the reaction mechanism of low-temperature CO oxidation. Previous mechanistic studies of CO oxidation at copper show that Cu<sup>0</sup> and Cu<sup>+</sup> share the same mechanism, while CO oxidation occurs at Cu<sup>2+</sup> sites by a different, and less efficient, mechanism [3]. The relative importance of Cu<sup>1+</sup> and Cu<sup>0</sup> that we observe is consistent with previous reports indicating that partially reduced Cu yields superior CO oxidation activity compared to fully reduced Cu [4,5,7] and the low-temperature CO binding site has been implicated as Cu<sup>+</sup> and not Cu<sup>0</sup> in reduced Cu [6]. Because Cu<sup>1+</sup>–CO is the main binding mode for CO at Cu/Aero surfaces (Fig. 5), even if Cu<sup>0</sup> content is increased, the surface sites are still predominantly Cu<sup>1+</sup> and thus Cu<sup>0</sup> content is not strongly linked to activity for CO oxidation.

The similarity in  $E_a$  between Cu/Aero catalyst and Cu/CP[photo]-A and -B (Table 2) indicates that the same reaction mechanism is occurring at active sites with the same chemical identity on both catalytic supports, while the aerogels benefit from a larger population of, or a superior ease of accessibility to, those active sites. The relative intensity of Cu–CO binding modes at Cu/Aero vs. Cu/CP catalyst highlights the dramatic difference in available surface area for CO binding (Fig. 5). Evaluating the surface area of supported Cu nanoparticles in Cu/Aero and Cu/CP by an electrochemical method [49] confirms an at least 2× increase in Cu surface area for Cu/Aero relative to Cu/CP (Table S3, Figure S9), in good agreement with IR spectroscopic differences in available CO binding sites on Cu/Aero and Cu/CP catalyst (Fig. 5). While Cu<sup>1+</sup> sites can be produced on both aerogel and CP supports, the only Cu/CP catalyst with low-temperature activity comparable to that of Cu/Aero was Cu/CP[photo]-A, the lone Cu/CP catalyst with abnormally high Cu<sup>0/1+</sup>:Cu<sup>2+</sup> ratio (Table S2). The fact that we always achieve high ratios of low-valent Cu on the aerogel supports (Cu<sup>0/1+</sup>:Cu<sup>2+</sup> > 1, Table S1) and do so with greater consistency than on the CP supports (i.e., without the need for photoreduction) demonstrates the efficacy of TiO<sub>2</sub> aerogels as a support for catalytic Cu nanoparticles.

In addition to the persistent fraction of majority low-valent Cu in Cu/Aero catalysts, the Cu/Aero catalyst may benefit from the placement of the active Cu species. The colocation of low-valent Cu sites and TiO<sub>2</sub> is critical to driving the Langmuir–Hinshelwood CO oxidation mechanism, as it places Cu-adsorbed and activated CO directly next to TiO<sub>2</sub>-adsorbed and -activated O<sub>2</sub> [50]. All of our observations point to a stabilization of low-valent Cu in Cu/Aero through extensive interfacial contact between Cu nanoparticles and the mesoporous TiO<sub>2</sub> support [15], giving us a form of Cu/TiO<sub>2</sub> that inherently co-locates activating sites.

#### 4. Conclusions

The enhanced Cu||TiO<sub>2</sub> interfacial contact in Cu/TiO<sub>2</sub> aerogels stabilizes Cu nanoparticles in oxidation states favorable for low-temperature CO oxidation. The multiple points of contact between supported Cu nanoparticles and the ~10-nm particles of the aerogel facilitate donation of electron density from the reducing oxide to the

supported Cu nanoparticles. Even in the absence of photoexcitation, aerogels yield a high Cu<sup>0/1+</sup>:Cu<sup>2+</sup> ratio and low-temperature CO oxidation not achieved on non-networked TiO<sub>2</sub> supports, which facilitate a lower interfacial density. More usefully, Cu/aerogels do not require strict UHV environments or an aggressive reduction step in order to retain the reduced forms of Cu needed to exhibit high rates of CO conversion at low temperature.

#### Acknowledgements

The authors acknowledge the Defense Threat Reduction Agency for support of this work. C.L.P. and A.M.P. gratefully acknowledge the U.S. National Research Council for support through a Naval Research Laboratory/National Research Council Postdoctoral Associateship.

#### Appendix A. Supplementary data

Supplementary material related to this article can be found, in the online version, at doi:<https://doi.org/10.1016/j.apcatb.2019.03.073>.

#### References

- [1] K. Mudiyanselage, S. Luo, H.Y. Kim, X. Yang, A.E. Barber, F.M. Hoffmann, J.A. Rodriguez, J.G. Chen, P. Liu, D.J. Stacchiola, *Catal. Today* 263 (2016) 4–10.
- [2] X.F. Yang, S. Kattel, K. Xiong, K. Mudiyanselage, S. Rykov, S.D. Senanayake, J.A. Rodriguez, P. Liu, D.J. Stacchiola, J.G. Chen, *Angew. Chem. Int. Ed.* 54 (2015) 11946–11950.
- [3] G.G. Jernigan, G.A. Somorjai, *J. Catal.* 147 (1994) 567–577.
- [4] C.-S. Chen, J.-H. You, J.-H. Lin, Y.-Y. Chen, *Catal. Commun.* 9 (2008) 2381–2385.
- [5] C.S. Chen, T.C. Chen, C.C. Chen, Y.T. Lai, J.H. You, T.M. Chou, C.H. Chen, J.-F. Lee, *Langmuir* 28 (2012) 9996–10006.
- [6] A.N. Il'ichev, D.P. Shashkin, V.A. Matyshak, V.N. Korchak, *Kinet. Catal.* 56 (2015) 198–206.
- [7] G.J. Wu, N.J. Guan, L.D. Li, *Catal. Sci. Technol.* 1 (2011) 601–608.
- [8] F. Bocuzzi, A. Chiorino, *J. Phys. Chem.* 100 (1996) 3617–3624.
- [9] F.H. Kaatz, V.G. Harris, D.R. Rolison, L. Kurihara, A.S. Edelstein, *Appl. Phys. Lett.* 67 (1996) 3807–3809.
- [10] F. Bocuzzi, A. Chiorino, G. Martra, M. Gargano, N. Ravasio, B. Carrozzini, *J. Catal.* 165 (1997) 129–139.
- [11] M.T. Greiner, L. Chai, M.G. Helander, W.-M. Tang, Z.-H. Lu, *Adv. Funct. Mater.* 22 (2012) 4557–4568.
- [12] C.M. Kalamaras, P. Panagiotopoulou, D.I. Kondarides, A.M. Efthathiou, *J. Catal.* 264 (2009) 117–129.
- [13] P. Panagiotopoulou, D.I. Kondarides, *J. Catal.* 267 (2009) 57–66.
- [14] A.E. Barber, X. Yang, H.Y. Kim, K. Mudiyanselage, M. Soldemo, J. Weissenrieder, S.D. Senanayake, A. Al-Mahboob, J.T. Sadowski, J. Evans, J.A. Rodriguez, P. Liu, F.M. Hoffman, J.G. Chen, D.J. Stacchiola, *Angew. Commun.* 53 (2014) 5336–5340.
- [15] P.A. DeSario, J.J. Pietron, T.H. Brintlinger, M. McEntee, J.F. Parker, O. Baturina, R.M. Stroud, D.R. Rolison, *Nanoscale* 9 (2017) 11720–11729.
- [16] N. Hüsing, U. Schubert, *Angew. Chem. Int. Ed.* 37 (1998) 22–45.
- [17] G.G. Dagan, M. Tomkiewicz, *J. Phys. Chem.* 97 (1993) 12651–12655.
- [18] P. Basu, T.H. Ballinger, J.T. Yates, *Rev. Sci. Instrum.* 59 (1988) 1321–1327.
- [19] B. Schumacher, Y. Denkowitz, V. Plzak, M. Kinne, R.J. Behm, *J. Catal.* 224 (2004) 449–462.
- [20] Y. Denkowitz, Z. Zhao, U. Hormann, U. Kaiser, V. Plzak, R.J. Behm, *J. Catal.* 251 (2007) 363–373.
- [21] P.B. Weisz, *Chem. Eng. Prog. Symp. Ser.* 55 (1992) 29.
- [22] D. Tahir, S. Tougaard, *J. Phys. Condens. Mat.* 24 (2012) 175002.
- [23] S.S. Zhang, B.Y. Peng, S.Y. Yang, H.J. Wang, H. Yu, Y.P. Fang, F. Peng, *Int. J. Hydrol. Energy* 40 (2015) 303–310.
- [24] T. Yamaguchi, E. Kazuma, N. Sakai, T. Tatsuma, *Chem. Lett.* 41 (2012) 1340–1342.
- [25] X. Guo, C. Hao, G. Jin, H.-Y. Zhu, X.-Y. Guo, *Angew. Chem. Int. Ed.* 53 (2014) 1973–1977.
- [26] I. Pastoriza-Santos, A. Sanchez-Iglesias, B. Rodriguez-Gonzalez, L.M. Liz-Marzan, *Small* 5 (2009) 440–443.
- [27] F. Gonzalez-Posada, R. Sellappan, B. Vanpoucke, D. Chakarov, *RSC Adv.* 4 (2014) 20659–20664.
- [28] K.P. Rice, E.J. Walker Jr., M.P. Stoykovich, A.E. Saunders, *J. Phys. Chem. C* 115 (2011) 1793–1799.
- [29] G.H. Chan, J. Zhao, E.M. Hicks, G.C. Schatz, R.P. Van Duyne, *Nano Lett.* 7 (2007) 1947–1952.
- [30] A. Marimuthu, J.W. Zhang, S. Linic, *Science* 339 (2013) 1590–1593.
- [31] D.B. Pedersen, S. Wang, S.H. Liang, *J. Phys. Chem. C* 112 (2008) 8819–8826.
- [32] M.D. Susman, Y. Feldman, A. Vaskevich, I. Rubinstein, *Chem. Mater.* 24 (2012) 2501–2508.
- [33] J.A. Jiménez, *J. Alloys Compd.* 656 (2016) 685–688.
- [34] E. Kazuma, T. Yamaguchi, N. Sakai, T. Tatsuma, *Nanoscale* 3 (2011) 3641–3645.
- [35] T. Ghossehali, M.A. Vesaghi, *Phys. B-Condens. Mater.* 406 (2011) 2678–2683.
- [36] A. Fohlsch, M. Nyberg, P. Bennich, L. Triguero, J. Hasselstrom, O. Karis,

L.G.M. Pettersson, A. Nilsson, *J. Chem. Phys.* 112 (2000) 1946–1958.

[37] C. Lamberti, A. Zecchina, E. Groppo, S. Bordiga, Probing the surfaces of heterogeneous catalysts by *in situ* IR spectroscopy, *Chem. Soc. Rev.* 39 (12) (2010) 4951–5001.

[38] T. Inoue, A. Fujishima, S. Konishi, K. Honda, *Nature* 277 (1979) 637–638.

[39] H. Yoneyama, *Catal. Today* 39 (1997) 169–175.

[40] M.J. Elser, T. Berger, D. Brandhuber, J. Bernardi, O. Diwald, E. Knozinger, *J. Phys. Chem. B* 110 (2006) 7605–7608.

[41] K.I. Hadjiivanov, G.N. Vayssilov, *Adv. Catal.* 47 (2002) 307–511.

[42] G. Busca, H. Saussey, O. Saur, J.C. Lavallee, V. Lorenzelli, *Appl. Catal.* 14 (1985) 245–260.

[43] V. Kozlov, E.A. Paukshtis, E.N. Savinov, *Appl. Catal. B* 24 (2000) L7–L12.

[44] L. Yi, G. Rammis, G. Busca, V. Lorenzelli, *J. Mater. Chem.* 4 (1994) 1755–1761.

[45] M. Casapu, A. Fisher, A.M. Gänzler, R. Popescu, M. Crone, D. Gerthes, M. Türk, J.-D. Grunwalt, *ACS Catal.* 7 (2017) 343–355.

[46] P.-A. Carlsson, L. Österlund, P. Thormählen, A. Palmqvist, E. Fridell, J. Jansson, M. Skoglundh, *Mater. J. Catal.* 226 (2004) 422–434.

[47] A.N. Subbotin, B.S. Gudkov, Z.L. Dykh, V.I. Yakerson, *React. Kinet. Catal. Lett.* 66 (1999) 97–104.

[48] A.N. Subbotin, B.S. Gudkov, V.I. Yakerson, S.V. Chertkova, E.Z. Golosman, G.V. Kozyreva, *Russ. J. Appl. Chem.* 74 (2001) 1506–1508.

[49] S.D. Giri, A. Sarkar, *Adv. Powder Technol.* 29 (2018) 3520–3526.

[50] S.D. Senanayake, N.A. Pappoe, T.-D. Nguyen-Phan, S. Luo, Y.Y. Li, W.Q. Xu, Z.Y. Liu, K. Mudiyanselage, A.C. Johnston-Peck, A.I. Frenkel, I. Heckler, D. Stacchiola, J.A. Rodríguez, *Surf. Sci.* 652 (2016) 206–212.